Double Armature Partitioned Stator Switched Flux PM Machine for Electric Vehicle Applications

Essam E. M. Mohamed
(https://orcid.org/0000-0003-0328-4865)

Abstract This paper investigates the performance of a partitioned stator switched flux permanent magnet machine that has double armature windings. The machine design is dedicated to electric vehicle applications. The modular structure, and the operation principles have been explained. Also, the design and optimization procedure for the machine including the rotor and stator number of poles and optimum parameters of the design have been clarified. The performance of the machine is compared with the conventional partitioned stator machine with a cylindrical inner stator and the salient inner stator machines, and the Prius interior permanent magnet machine. The partitioned stator machines have the same main parameters which are globally optimized for optimum average torque. The comparison is based on the electromagnetic performance in the open-circuit and on-load analysis. The 2D finite element results show the superior performance of the double armature portioned stator machine based on the highest average torque, the minimum cogging torque, and the best torque-current density and torque per PM volume characteristics.

1 Introduction

Recently, environmental concerns including global warming, climate change, greenhouse gas emissions…etc., motivate research in the direction of replacing vehicles with internal combustion engines with electric vehicles (EV) or hybrid electric vehicles (HEV). EV/HEV offers improved fuel economy with the help of optimized engine operation and recovered kinetic energy during braking [1]. In addition, EVs/HEVs can be supplied and/or charged from renewable energy systems such as PV and wind energy, hence decreases the dependence on ICEVs, hence decrease the dependency on the depleted fuel oil.

To satisfy vehicle and traction applications requirements, electric machine drives should offer improved characteristics including [2-4]:

- High torque/power density
- High starting torque for low speeds and hill-climbing
- High power at high speed
- Wide speed range
- High efficiency over wide speed and torque ranges
- High intermittent overload capability
- High reliability and robustness
- High EMC and low acoustic noise
- Reasonable cost

The Switched Reluctance Motor (SRM) has a simple and sturdy design, it offers high-speed fault-tolerant operation [5]. However, its operation principle involves high acoustic noise and low power factor [6].   Although the rotor has no active components, PMs, or field-windings, and the stator employs concentrated windings, the SRM offers similar power density and efficiency to IM. Another disadvantage is the high torque ripples in the low-speed region and efficient operation ($\eta >$ 0.85) is limited to the high-speed region [7]. Also, the SRM is fed by an asymmetric configuration H-bridge inverter, rather than the conventional voltage source inverter. So far, the use of SRM is limited to the Land Rover Defender that employs a 70 kW motor.

Induction motors (IM) provide robust construction, low cost, good efficiency, good flux-weakening characteristics, and familiarized control techniques [6, 8, 9]. However, the current circulates in both the stator and rotor windings, hence losses and temperature rise [6, 9].

Permanent magnet synchronous motors (PMSM) represent the core of HEVs and EVs basically due to their superior efficiency, high power and torque density, and wide torque-speed characteristics [10]. These merits encourage big vehicle manufacturers to adopt the PMSM in more than 80% of the installed EV propulsion systems from 2006 to 2016 [11]. Based on **Fig. 1**, the installed DC motors and SRM motors are vanished by the year 2016. While the IM share is almost constant, but the trend shows the dominance of the PMSM over time [11].

Partitioned stator (PS) machines solve the permanent magnet and armature winding space conflict [12, 13]. The conventional PS, **Fig. 2(a)**, has been previously designed and the performance was compared with the Prius interior permanent magnet (IPM) machine, **Fig. 2(b)**, [14]. The study shows the distinctive merits of the PS for EV applications compared with the IPM machine. Although the proposed 12/10 poles PS design offers two times the peak electromagnetic torque of the IPM machine, it employs five times the PM volume. The salient inner stator PS machine was proposed by [13] for direct-drive wind generator applications. The proposed design reduces the inner stator core material by 50% while maintaining the same electromagnetic performance. Four different C-core/E-core topologies were studied in [12], the comparison shows that the salient inner stator machine with inner C-core and outer E-core exhibits the best performance based on the electromagnetic performance,

power loss and efficiency. Furthermore, the double armature PS design was introduced in [15], however, the proposed design was dedicated for direct-driven wind generator applications. In addition, the dual armature stator with biased PM excitation was introduced in [16] to improve the torque density. Two partitioned-stator and two partitioned rotor machines were compared in [17], the study aimed to compare the performance of the four machines under EV applications, but none of the studied machines has a double armature design.

This paper study the performance of a PS machine with two armature windings, namely the double armature PS machine (DA-PS). The design and operation principles of the machine are explained, and the electromagnetic performance is compared with the conventional cylindrical inner stator PS (CR-PS) and the salient inner stator PS (SA-PS) machines having the same main design dimensions. Besides, the performance of the three PS machines is compared with the Prius IPM machine [18].
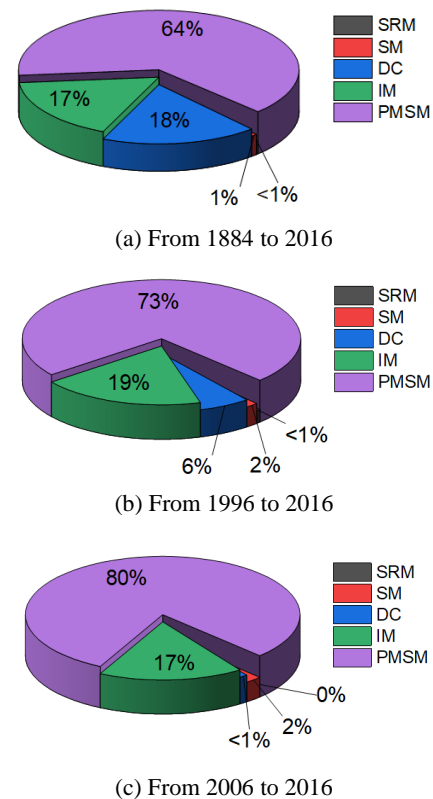

(a) From 1884 to 2016

(b) From 1996 to 2016

(c) From 2006 to 2016

Fig. 1 Percentage of installed electric machines in EV applications [11].

This paper is classified as follows; Section 1 presents the introduction, Section 2 provides the modular structure of the machine, Section 3 explains the operation principles, Section 4 discusses the machine design and optimization procedure, Section 5 presents a comparison based on the electromagnetic performance, and finally, Section 6 provides the conclusion.
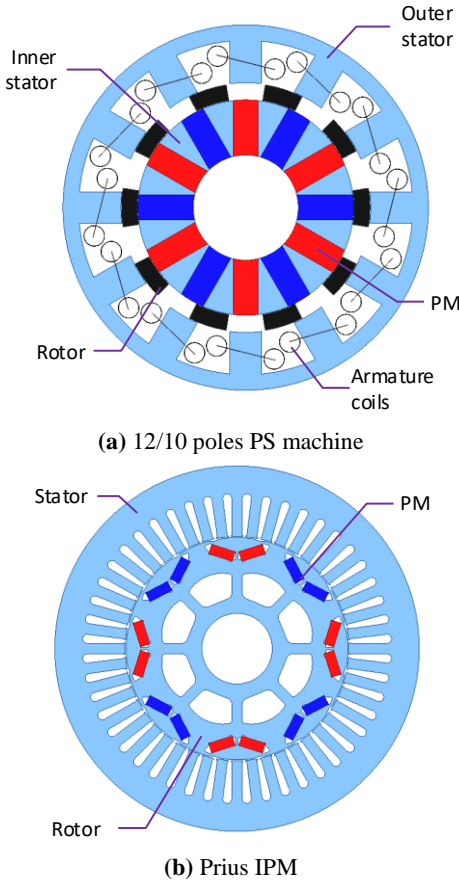

(a) 12/10 poles PS machine

(b) Prius IPM

Fig. 2 PS and IPM machines [14].

2 Modular Structure of the PS Machines

The CR-PS machine with the C-core design has six inner/outer stator poles and 13 rotor poles. Hence, the outer stator will be as shown in **Fig. 3** and the inner stator will be as shown in **Fig. 5(a)**. The SA-PS machine has the same outer stator as the CR-PS machine, while the inner stator has V-shaped iron cores, as given in **Fig. 5(b)**. The width of the inner stator teeth is calculated to develop maximum electromagnetic torque, hence the same performance of the CR-PS machine is obtained with reduced iron core material. The free space

obtained by the SA-PS machine is filled by the second set of windings, namely the inner stator winding set, hence the dual winding structure is obtained using the modular structure shown in **Fig. 5(c)**.

For all the three PS machines the rotor is constructed by iron poles as shown in **Fig. 4.** The concentrated winding is applied on all the three PS machines to reduce the copper loss and the winding configuration is set according to the coils back-EMF phasors given in **Fig. 6(a)** for the CR-PS and the SA-PS machines and **Fig. 6(b)** for the DA-PS machine. The final structure of the three PS machines is shown in **Fig. 7.** The **Appendix** describes the assembly of all the components of the PS machines.
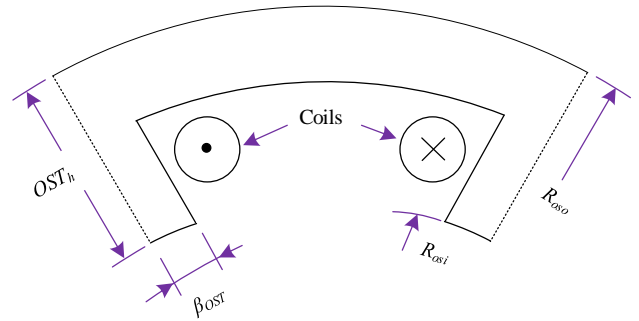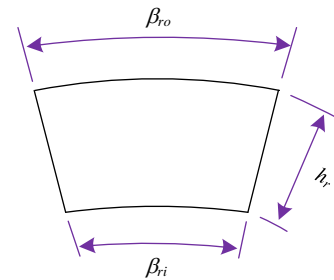

Fig. 3 Outer stator, CR-PS, SA-PS and DA-PS.

Fig. 4 One rotor-pole, CR-PS, SA-PS, and DA-PS.

(a) Inner stator, CR-PS

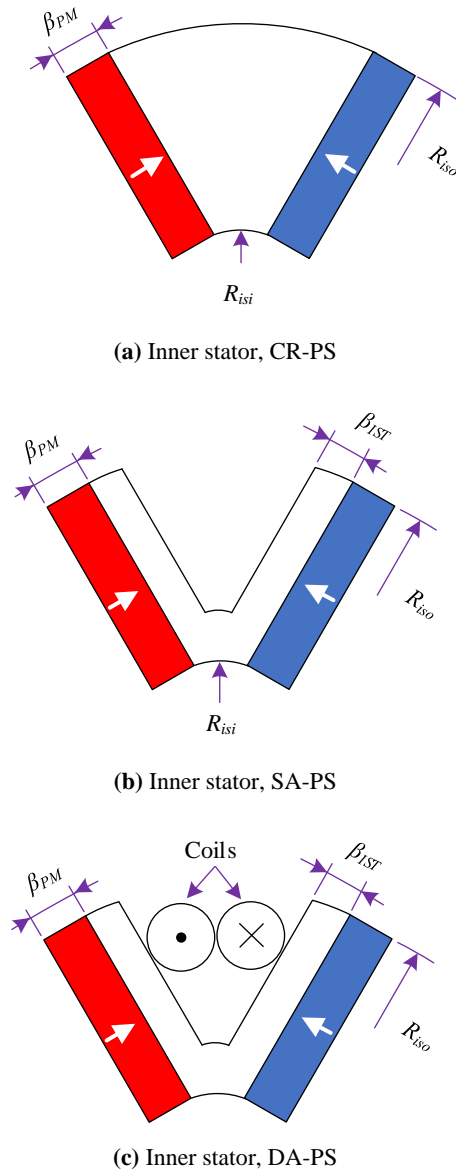**(b)** Inner stator, SA-PS

(c) Inner stator, DA-PS

Fig. 5 The modular structure of the inner stator.

3 Operation Principles

The sinusoidal flux-linkage of Coil (1), as shown in **Fig. 8**, is obtained by the movement of the rotor poles. At zero electrical position, as explained by the open-circuit field distribution given in **Fig. 9(a)**, the rotor pole links the maximum negative flux-linkage. With the movement of the rotor to the 90° position, **Fig. 9(b)**, two-rotor poles short-circuit the flux of Coil (1), and zero flux-linkage is obtained.

At 180° electrical position, **Fig. 9(c)**, the next rotor pole links the maximum positive flux-linkage. In 270° electrical position, **Fig. 9(d)**, one rotor pole short-circuits the flux of Coil (1), and zero flux-linkage is obtained. With the continuous movement of the rotor, sinusoidal flux-linkage is obtained on the three machines. It can be seen in **Fig. 8**, the CR-PS and the SA-PS machines provide very close flux-linkage, as they have similar outer stators. For the DA-PS machine, the flux links two stator coils, i.e., the outer and inner stator coils.

4 Machine Design and Optimization

4.1 Rotor/Stator Pole Combinations

The rotor/stator pole combination is selected based on Eq. (1) [19]. For $N_s = 6$, N_r can be assumed as 11, 13 for $k = 1$ and 10, 14 for $k = 2$…etc. To select the final rotor/stator poles combination, four 2D finite element analysis (FEA) models of the DA-PS machines were applied based on the same design parameters, $N_s = 6$, and rotor poles of 10, 11, 13, and 14.
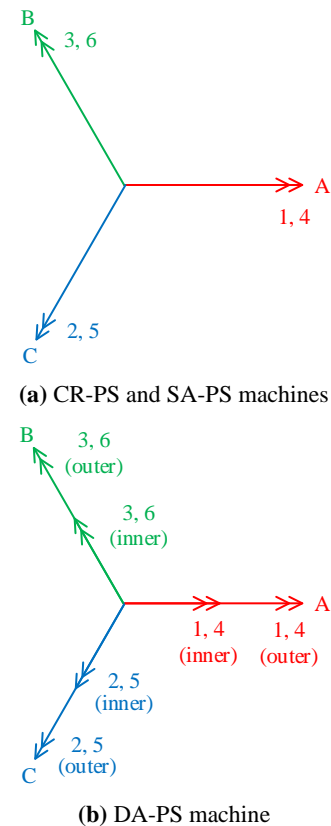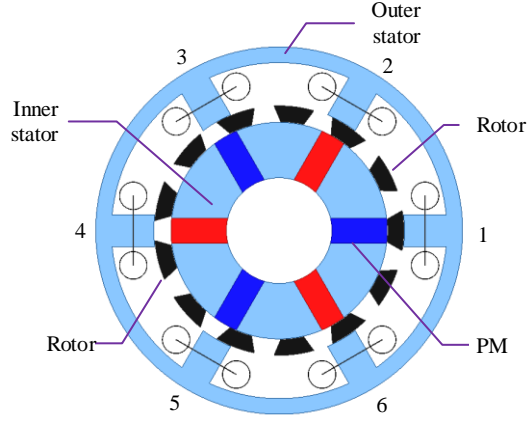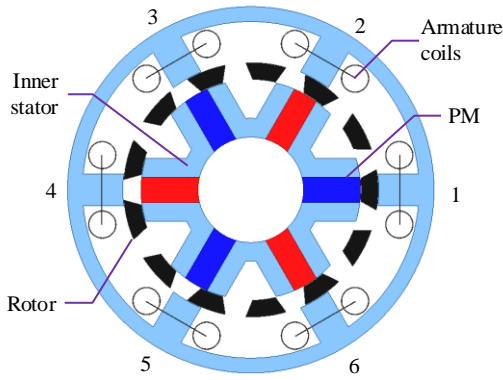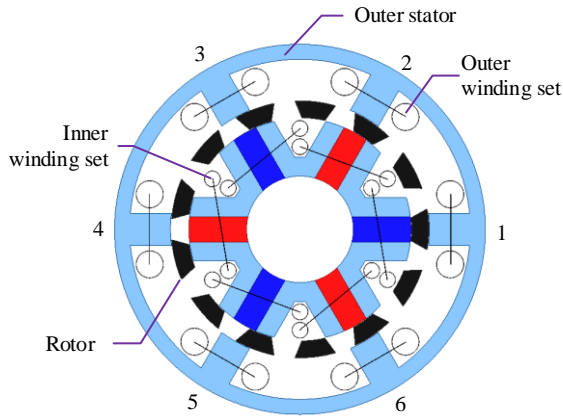

(a) CR-PS and SA-PS machines

(b) DA-PS machine

Fig. 6 Coil back-EMF phasors of the PS machines.

(a) Cylindrical inner stator PS-SFPM

(b) Salient inner stator PS-SFPM

(c) Double armature Salient inner stator PS-SFPM

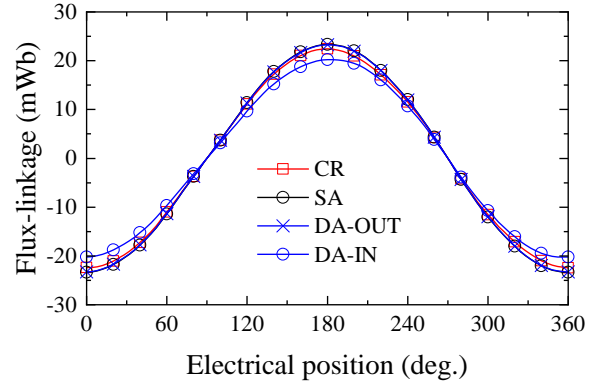**Fig. 7** Structure of the PS machines.

Fig. 8 Coil (1) flux-linkage.

The electromagnetic performance of the four machines is shown in **Fig. 10** and **Fig. 11**. As shown from the phase back-EMF given in **Fig. 10(a)** and the harmonic spectra given in **Fig. 10(b)**, the phase back-EMF of $N_r = 11$ and $N_r = 13$ is very close with a fundamental voltage of 92.5 V and 96.8 V and THD of 4.2% and 4.1% for $N_r = 11$ and $N_r = 13$, respectively. Whilst the phase voltage fundamental of 51.3 V and 57.9 V and THD of 10.0% and 7.0% for $N_r = 10$ and $N_r = 14$, respectively. The high THD of the 10- and 14-rotor poles is due to the unsymmetrical back-EMF waveform, see **Fig. 10(a)**, where Eq. (3) is satisfied for symmetrical waveforms.

$$N_r = 2N_s \pm k \quad N_r = 2N_s \pm k, \, k = 1, 2, \dots \quad (1)$$

$$T_{rp} = \frac{T_{max} - T_{min}}{T_{avg}} \quad (2)$$

where T_{max}, T_{min}, and T_{avg} are the maximum, minimum, and average torque.

$$\frac{N_s}{HCF_{(N_s,N_r)}} = even\ number \quad (3)$$

where HCF is the highest common factor.

The cogging torque is given in **Fig. 11(a)**, it can be seen that the peak-to-peak cogging torque equals 66.7 and 75.2 Nm for $N_r = 10$ and $N_r = 14$, respectively, and the peak-to-peak cogging torque for $N_r = 11$ is 23.7 Nm while the lowest peak-to-peak cogging torque of 8.8 Nm is for $N_r = 13$. The average torque at the same current density of 5 A/mm² is shown in **Fig. 11(b)**. It can be seen that the average torque for $N_r = 13$ is equal to 185.2 Nm with torque ripples (T_{rp}) = 4.6%, where the torque ripples are calculated by (2). The average torque and the torque ripples are 173.8 Nm and 23.9%, 135.5 Nm and 76.4%, and 111.1 Nm and 84.8% for N_r equals 11, 14, and 10,

respectively. The machine with a rotor number of poles N_r = 13 exhibits the best performance based on the highest average electromagnetic torque and minimum torque ripples. Finally, **Fig. 11(c)** shows the developed torque vs. the current density. It can be seen the superior performance of the machine with N_r = 13 all over the current density range.

Based on the previous analysis and electromagnetic performance the rotor/stator poles combination is selected as 6/13.

4.2 Optimum Inner Stator Teeth Width

For the DA-PS, the space conflict between inner stator teeth width, inner armature coils space, and PM width can be optimized based on maximum average torque. **Fig. 12** shows the electromagnetic torque vs. the PM width (β_{PM}) and the inner stator teeth width (β_{IST}). It is evident that the maximum torque is obtained at β_{PM} = 18 mm and β_{IST} = 13.5 mm.

4.3 Parameters Optimization

This section describes the design and optimization of the main design parameters of the three PS machines. For the sake of comparison, the main design parameters of the Prius IPM machine is applied to the three PS machines, hence the axial length and the machines' outer radius are set as 50.8 mm and of 132 mm, respectively.

Next, the initial design parameters of the PS machines were set as 50% of full value, for example, the outer stator teeth arc (β_{OST}) is set as (4), the rotor inner (β_{ri}) and outer (β_{ro}) arcs are set as (5), and the split ratio (S_r), which is defined as the ratio of the outer air-gap radius (R_{go}) with respect to the outer machine radius (R_o) [20], is set to 0.7 as in (6). For the SA-PS, the PM arc (β_{PM}) and the inner stator teeth arc (β_{IST}) are initially calculated based on the outer rotor SF machines principles as given in (7) [21-23].

$$\beta_{OST} = 0.5 \cdot \frac{2\pi}{N_s} = \frac{\pi}{N_s} \tag{4}$$

$$\beta_{ri} = \beta_{ro} = 0.5 \cdot \frac{2\pi}{N_r} = \frac{\pi}{N_r} \tag{5}$$

$$S_r = \frac{R_{go}}{R_o} = 0.7 \tag{6}$$

$$\beta_{PM} = \beta_{IST} = \frac{1}{3} \cdot \frac{2\pi}{N_s} \tag{7}$$

where β_{OST} is the outer stator teeth arc, β_{ri} and β_{ro} are rotor inner and outer arcs, respectively. S_r is the split, R_{go} is the outer air-gap radius, and R_o is the outer machine radius. β_{PM} and β_{IST} are the PM arc and the inner stator teeth arc, respectively.

Next, the initial design parameters were applied to the machine's 2D finite element models which are developed by the ANSYS MAXWELL 2D software, then the design parameters have been globally optimized using the genetic algorithm to obtain the highest average torque (T_{ave}) with minimum peak-to-peak torque ripples (T_{rp}). The optimization process is done at a current density of 5 A/mm^2. The objectives and cost functions are given as follows.

$$G_1 = 1 + (100 - T_{ave}) \times (9/20) \tag{8}$$

$$G_2 = 1 + (T_{rp} - 0.5) \times (9/9.5) \tag{9}$$

$$Cost = 1 \times (G_1 - 1)^2 + 1 \times (G_2 - 1)^2 \tag{10}$$

where the weight of each goal is unity.

Finally, a parametric analysis is performed to refine the critical design parameters such as S_r, β_{PM}, β_{ri}, βro, h_r, β_{OST}, and OST_h. The final design parameters are presented in **Table 1**.

5 Performance Comparison

5.1 The Open-circuit Performance

Fig. 13 shows the cogging torque of the PS machines. The DA and the CR machines exhibit similar cogging torque with peak-to-peak cogging torque of 8.8 and 8.5 Nm, respectively. The SA machine exhibits the higher peak-to-peak cogging torque of 10.2 Nm, and finally, the IPM machine provides the lowest peak-to-peak cogging torque of 1.5 Nm. The phase back-EMF is shown in **Fig. 14(a)** at a speed of 1500 rpm and the harmonic spectra are shown in **Fig. 14(b)**. The fundamental of the DA, the SA, the CR, and the IPM machines is 94.1 V, 94.5 V, 90.7 V, and 78.9 V, respectively. The DA machine has the inner winding fundamental of 82.3 V. The THD for the PS machines is 3.22%, 3.27%, and 3.5% for the DA, the SA, and the CR machines, respectively. The IPM machine has the highest THD of 16.5% due to the high third harmonic component, see **Fig. 14(c)**.
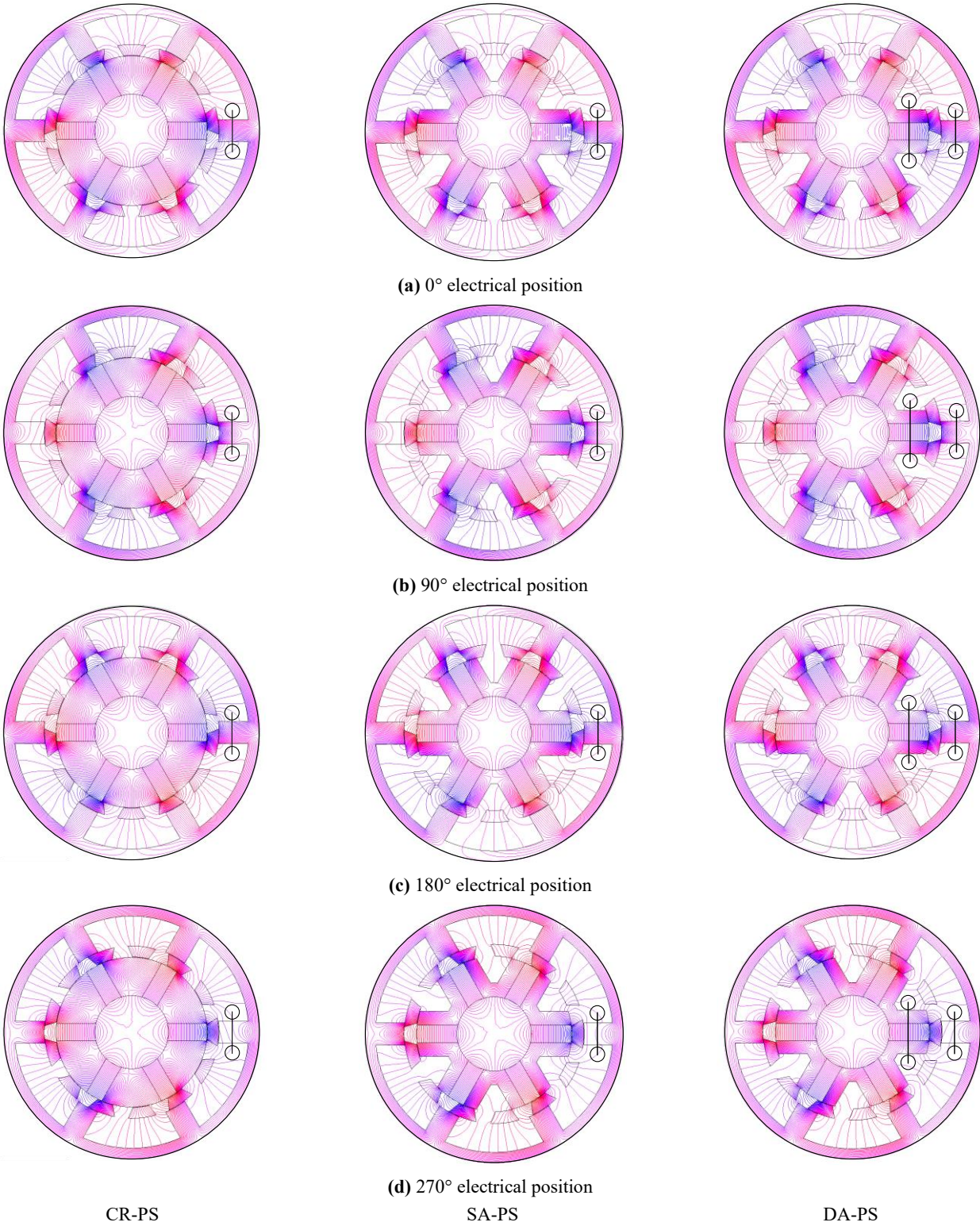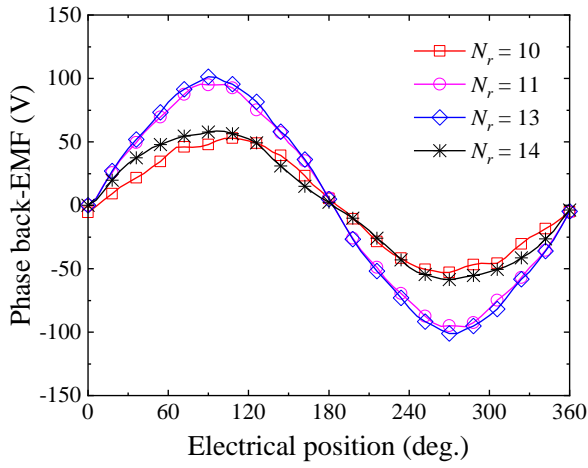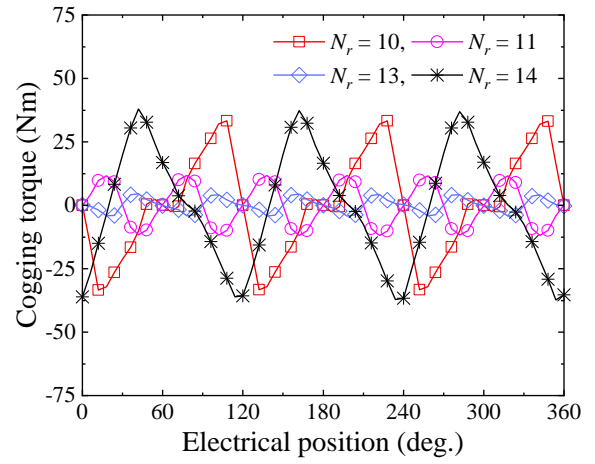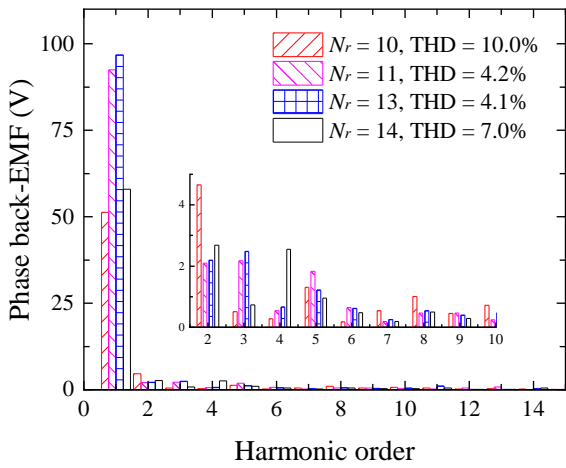
(a) 0° electrical position

(b) 90° electrical position

(c) 180° electrical position

(d) 270° electrical position

CR-PS   SA-PS   DA-PS

Fig. 9 Open-circuit field distribution.

(a) Back-EMF

(b) Harmonic spectra
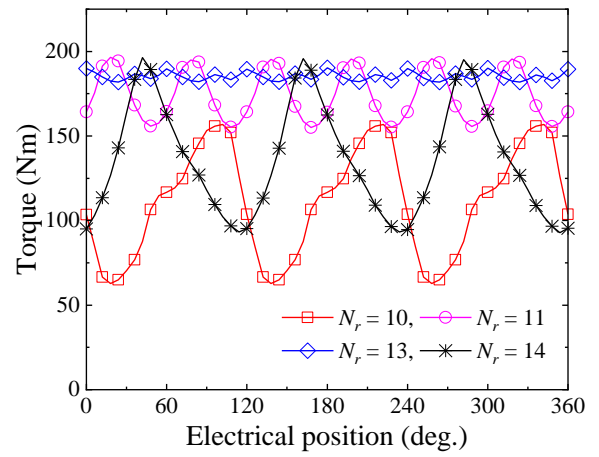
Fig. 10 Back-EMF of the DA-PS machine with $N_s = 6$ and different number of rotor poles

(a) Cogging torque
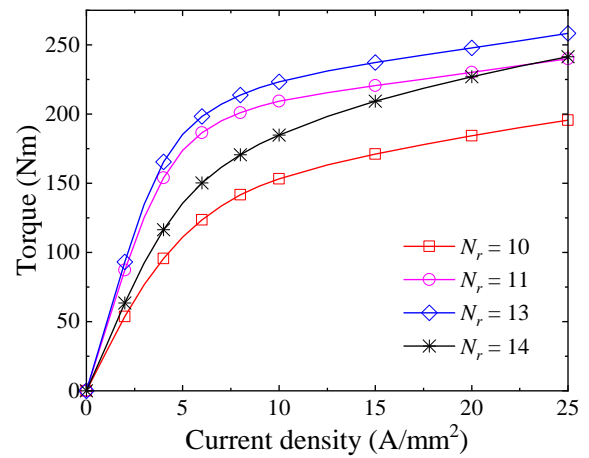
(b) Developed torque

(c) Developed torque vs. current density

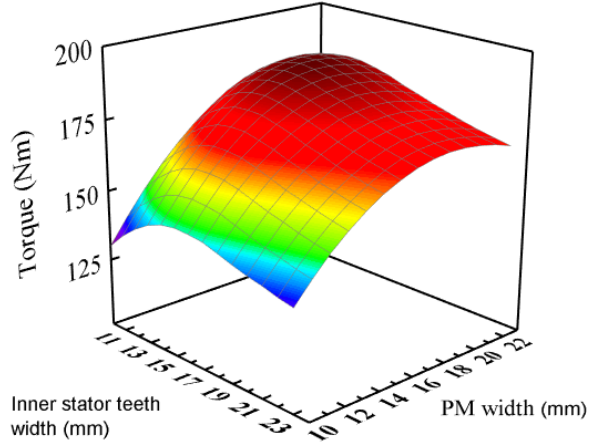**Fig. 11** Torque of the DA-PS machine with $N_s = 6$ and different number of rotor poles.

Fig. 12 Optimal inner stator teeth width (β_{IST}).

Table 1 Final design parameters.

Parameter	DA	SA	CR
Number of rotor poles, N_r		13	
Number of stator poles, N_s		6	
Inner air-gap, g_i		0.5 mm	
Outer air-gap, g_o		0.5 mm	
Axial length, L_a		50.8 mm	
Outer radius, R_o		132 mm	
Inner radius, Ro		38 mm	
Coil number of turns, N_c		21	
Split ratio, S_r		0.69	
Packing factor, k_{pf}		0.5	
PM dimensions, mm	18x41.6		18x40.4
Rotor radial length	12.1 mm		11.4 mm
Inner stator teeth width, mm	13.5	14	--
Rotor inner arc		12°	
Rotor outer arc		18.4°	
Outer teeth height ratio		29.25 mm	
Outer slot ratio, OS_r		45.7°	
PM remanence, B_r		1.2	
Rated speed, Ω		1500 rpm	

5.2 The On-load Performance

The torque vs. the current angle as shown in **Fig. 15** shows that the maximum torque for the PS machines occurs at 10°, however, zero d-axis current control could be applied to simplify the controller algorithm. In contrast, for the IPM machine, the maximum torque occurs at 30°, hence more complicated algorithms are mandatory to assure maximum torque per ampere operation. The torque vs. the current density is shown in **Fig. 16**. It can be seen that the DA machine exhibits the highest torque up to 12.5 A/mm² hereafter the SA machine torque will be a little higher due to the increased armature reaction in the DA machine. The CR machine exhibits the lowest torque among the PS machines, while the IPM machine develops the lowest torque through the whole current density range.

Fig. 17 shows the electromagnetic torque for the four machines at a current density of 5 A/mm², the CR-PS, and the SA-PS develops an average electromagnetic torque of 166.0 Nm and 170.8 Nm, respectively. The IPM machine develops 43.6 Nm, while the DA-PS develops the highest average electromagnetic torque of 185.2 Nm. Also, the DA-PS machine exhibits the highest torque per PM volume for current density up to 10 A/mm2 as shown in Fig. 18. But for current densities higher than 10.0 A/mm², the armature reaction of the PS machines increases that decreases the developed torque and the IPM exhibits higher developed torque. The percent of cogging torque to the average electromagnetic torque: 6.1%, 5.0%. 3.4%, 4.8%, for the CR-PS, the SA-PS, the IPM, and the DA-PS machines, respectively.
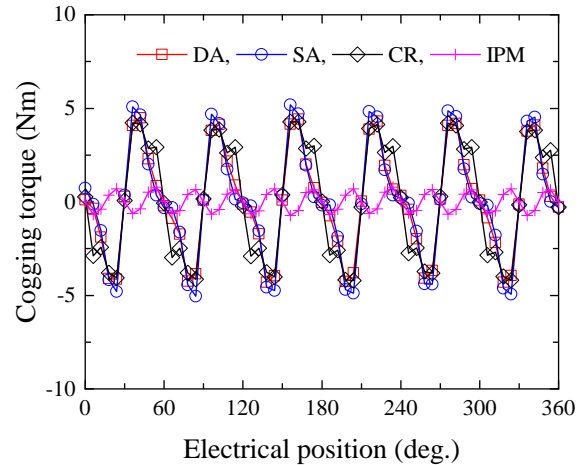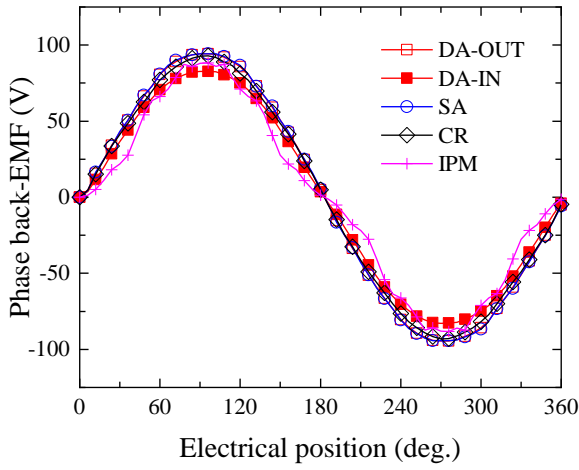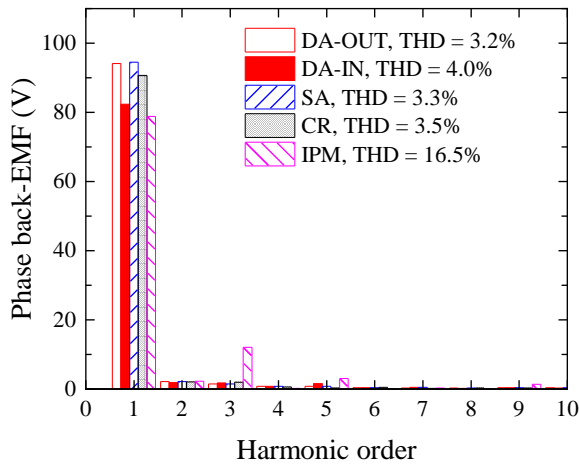

Fig. 13 Open-circuit performance—Cogging torque.

(a) Back-EMF

(b) Harmonic spectra

Fig. 14 Open-circuit performance—Back-EMF.
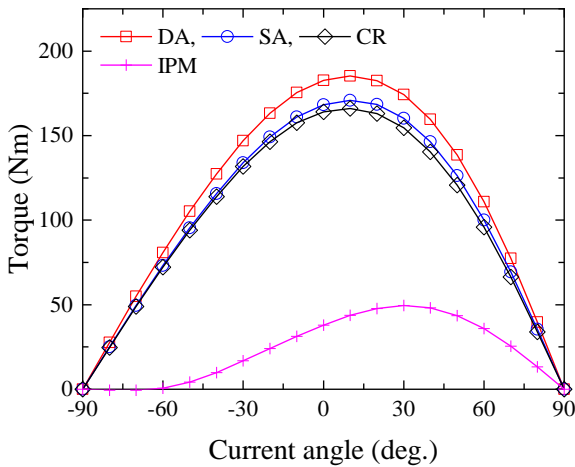

Fig. 15 Torque vs. current angle.
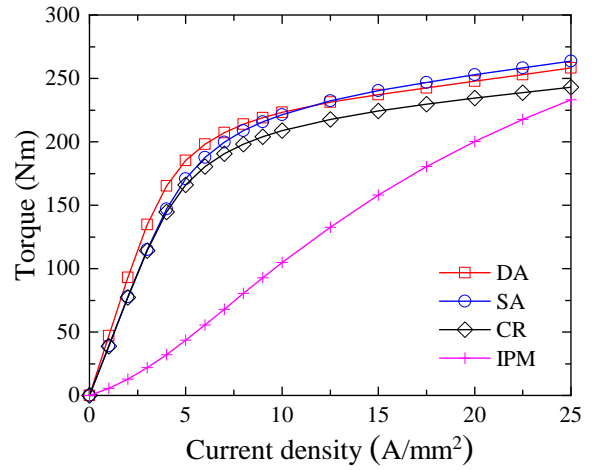

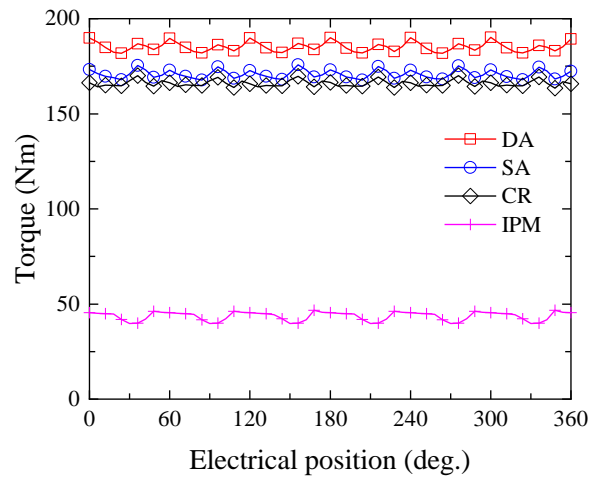
Fig. 16 Torque vs. current density.

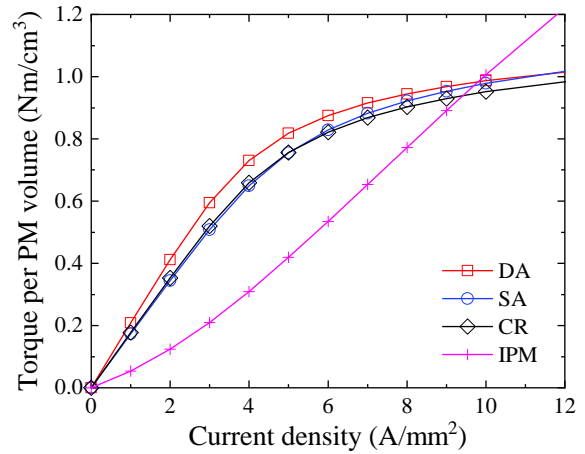
Fig. 17 Electromagnetic torque.

Fig. 18 Torque per PM volume vs. the current density.

6 Conclusion

In this paper, the DA-PS machines have been designed for EV applications. The DA-PS design incorporates two armature windings sets. The first is accommodated by the outer stator, while the second set is accommodated in the salient inner stator. The operation principles, the machine design, and the optimization procedure have been explained for the DA-PS machine. The performance is compared to the CR-PS, the SA-PS, and the Prius IPM machine based on the open-circuit and the on-load performance. The comparison shows the superior performance of the DA-PS design based on the cogging torque, the average developed torque, and the torque per PM volume.

References

[1] C. C. Chan, "The state of the art of electric, hybrid, and fuel cell vehicles," *Proceedings of the IEEE,* vol. 95, no. 4, pp. 704-718, 2007.

[2] K. Chau, C. C. Chan, and C. Liu, "Overview of permanent-magnet brushless drives for electric and hybrid electric vehicles," *IEEE Transactions on industrial electronics,* vol. 55, no. 6, pp. 2246-2257, 2008.

[3] Z. Zhu and D. Howe, "Electrical machines and drives for electric, hybrid, and fuel cell vehicles," *Proceedings of the IEEE,* vol. 95, no. 4, pp. 746-765, 2007.

[4] M. Cheng, L. Sun, G. Buja, and L. Song, "Advanced electrical machines and machine-based systems for electric and hybrid vehicles," *Energies,* vol. 8, no. 9, pp. 9541-9564, 2015.

[5] K. M. Rahman, B. Fahimi, G. Suresh, A. V. Rajarathnam, and M. Ehsani, "Advantages of switched reluctance motor applications to EV and HEV: design and control issues," *IEEE Transactions on Industry Applications,* vol. 36, no. 1, pp. 111-121, 2000, doi: 10.1109/28.821805.

[6] Z. Yang, F. Shang, I. P. Brown, and M. Krishnamurthy, "Comparative Study of Interior Permanent Magnet, Induction, and Switched Reluctance Motor Drives for EV and HEV Applications," *IEEE Transactions on Transportation Electrification,* vol. 1, no. 3, pp. 245-254, 2015, doi: 10.1109/TTE.2015.2470092.

[7] T. Finken, M. Felden, and K. Hameyer, "Comparison and design of different electrical machine types regarding their applicability in hybrid electrical vehicles," in *2008 18th International Conference on Electrical Machines*, 2008: IEEE, pp. 1-5.

[8] M. J. Akhtar and R. K. Behera, "Optimal design of stator and rotor slot of induction motor for electric vehicle applications," *IET Electrical Systems in Transportation,* vol. 9, no. 1, pp. 35-43, 2018.

[9] A. K. Singh, A. Dalal, and P. Kumar, "Analysis of induction motor for electric vehicle application based on drive cycle analysis," in *2014 IEEE International Conference on Power Electronics, Drives and Energy Systems (PEDES)*, 2014: IEEE, pp. 1-6.

[10] I. López, E. Ibarra, A. Matallana, J. Andreu, and I. Kortabarria, "Next generation electric drives for HEV/EV propulsion systems: Technology, trends and challenges," *Renewable and Sustainable Energy Reviews,* vol. 114, p. 109336, 2019.

[11] A. M. Bazzi, Y. Liu, and D. S. Fay, "Electric Machines and Energy Storage: Over a century of technologies in electric and hybrid electric vehicles," *IEEE Electrification Magazine,* vol. 6, no. 3, pp. 49-53, 2018.

[12] E. E. M. Mohamed, "Electromagnetic Performance of Partitioned Stator PM Machines with Dual C-core/E-core Topologies," in *2017 Eighteenth International Middle East Power Systems Conference (MEPCON)*, 19-21 Dec. 2017 2016.

[13] E. E. M. Mohamed, D. Reigosa, and Z. Q. Zhu, "Novel salient inner stator Partitioned Stator Switched Flux PM machine," in *2016 Eighteenth International Middle East Power Systems Conference (MEPCON)*, 27-29 Dec. 2016 2016, pp. 523-528, doi: 10.1109/MEPCON.2016.7836941.

[14] Z. Zhu and H. Hua, "A partitioned stator permanent magnet machine for HEV/EV applications," in *Sustainable Mobility Applications, Renewables and Technology (SMART), 2015 International Conference on*, 2015: IEEE, pp. 1-7.

[15] E. E. Mohamed, M. S. Saeed, and A. I. Ali, "Dual Three-Phase Partitioned Stator Flux-Switching PM Machine for Wind Generating Systems," in *2018 Twentieth International Middle East Power Systems Conference (MEPCON)*, 2018: IEEE, pp. 992-997.

[16] H. Yang *et al.*, "Novel dual-stator machines with biased permanent magnet excitation," *IEEE Transactions on Energy Conversion,* vol. 33, no. 4, pp. 2070-2080, 2018.

[17] M. Saeed and E. E. Mohamed, "Partitioned Topologies of Switched Flux Permanent Magnet Machines for Electric Vehicles," *International Journal of Computer Applications,* vol. 179, no. 41, pp. 23-30, 2018.

[18] T. A. Burress *et al.*, "Evaluation of the 2010 Toyota Prius hybrid synergy drive system," Oak Ridge National Laboratory (ORNL); Power Electronics and Electric Machinery Research Facility, 2011.

[19] C. Awah, Z. Zhu, Z. Wu, and D. Wu, "High torque density magnetically-geared switched flux permanent magnet machines," in *Ecological Vehicles and Renewable Energies (EVER), 2015 Tenth International Conference on*, 2015: IEEE, pp. 1-6.

[20] D. J. Evans and Z. Q. Zhu, "Novel partitioned stator switched flux permanent magnet machines," *IEEE Transactions on Magnetics,* vol. 51, no. 1, pp. 1-14, 2015, doi: 10.1109/TMAG.2014.2342196.

[21] W. Fei, P. C. K. Luk, J. Shen, and Y. Wang, "A novel outer-rotor permanent-magnet flux-switching machine for urban electric vehicle propulsion," in *Power Electronics Systems and Applications, 2009. PESA 2009. 3rd International Conference on*, 20-22 May 2009 2009, pp. 1-6.

[22] E. E. M. Mohamed, "Outer rotor flux-switching permanent magnet generator for direct drive wind energy applications " presented at the 16th International Middle-East Power Systems Conference - MEPCON'2014., Ain Shams University, Cairo, Egypt., December 23 - 25, 2014., 2014.

[23] Y. Wang, M. J. Jin, J. X. Shen, W. Z. Fei, and P. C. K. Luk, "An outer-rotor flux-switching permanent magnet machine for traction applications," in *2010 IEEE Energy Conversion Congress and Exposition*, 12-16 Sept. 2010 2010, pp. 1723-1730, doi: 10.1109/ECCE.2010.5618120.

Appendix

Assembly of the PS machine

The assembly of PS machines can be explained with the help of the figure below. The outer stator (1) accommodates the armature soils (2) while the inner stator (3) accommodates the PMs (4). The rotor-poles (5) are constructed by iron pieces that can turn between the two stators with the help of two air gaps. An epoxy resin (6) is employed to enclose the rotor-poles and an aluminum plate and ring (7) are used to fix the rotor assembly to the shaft (8). The shaft connects the PS machine to the mechanical load. The outer stator is fixed to the machine frame (9) while the inner stator is attached to the end bracket (10).
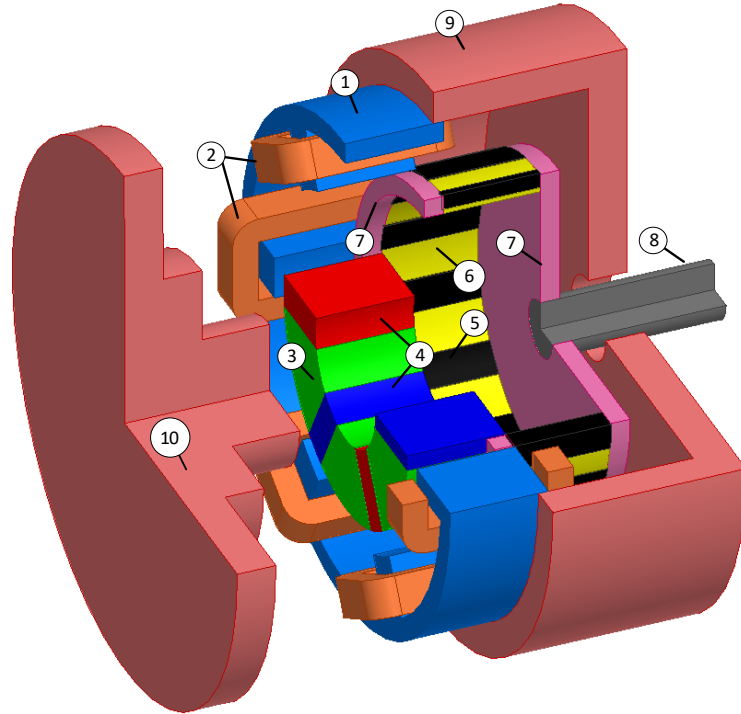
(1) Outer stator	(6) Epoxy resin
(2) Armature coils	(7) Ring and plate
(3) Inner stator	(8) Shaft
(4) PMs	(9) Frame
(5) Rotor poles	(10) End bracket